Nanopore Analysis of Individual RNA/Antibiotic Complexes

Meni Wanunu,[†,*] Swati Bhattacharya,[‡] Yun Xie,[§] Yitzhak Tor,[§] Aleksei Aksimentiev,[‡,*] and Marija Drndic[†,∥,*]

[†]Departments of Physics and Chemistry/Chemical Biology, Northeastern University, Boston, Massachusetts 02115, United States, [‡]Department of Physics, University of Illinois, Urbana, Illinois 61801, United States, [§]Department of Chemistry and Biochemistry, University of California, San Diego, La Jolla, California 92093, United States, and [∥]Department of Physics and Astronomy, University of Pennsylvania, Philadelphia, Pennsylvania

ABSTRACT

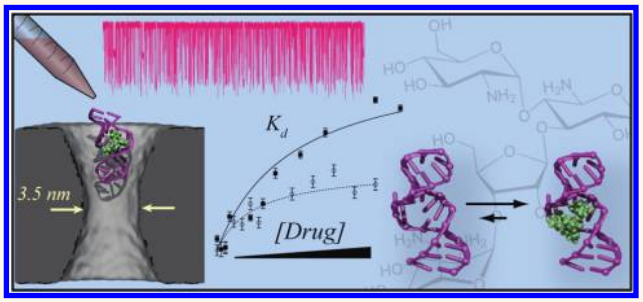

Nanopores in thin solid-state membranes are used to rapidly analyze individual RNA/drug complexes. The interactions of a truncated A-site RNA model of the prokaryotic ribosome with aminoglycoside antibiotics are characterized by passing individual molecules through a 3–3.5 nm diameter pore fabricated in a 8–10 nm thick silicon nitride membrane. Complexes of the A-site RNA with aminoglycosides can be distinguished from unbound A-site based on the ion current signatures produced as they pass through the nanopores. Counting the fraction of free and drug-bound molecules affords label-free drug–RNA binding isotherms consistent with literature reports and with data generated using independent fluorescence-based assays. Our measurements are supported by molecular dynamics simulations, which illustrate the relationship between the ionic current and complexation of the A-site RNA with paramomycin, a prototypical aminoglycoside antibiotic.

KEYWORDS: antibiotics · single-molecule · molecular dynamics · A-site · rRNA · drug discovery

Ribonucleic acid molecules have enormous potential as drug targets for numerous RNA-mediated diseases and bacterial/viral infections.[1–4] As the vast majority of discovery tools are focused on protein targets, there is a clear need for experimental and computational development of tools for discovery of RNA targeting drugs.[5] This is particularly true for antibacterials, as many bacterial strains have evolved resistance to contemporary antibiotic treatments,[6] and antibiotics currently in clinical use might become obsolete in the near future. New methods for probing RNA/drug interactions that are fast, accurate, and sensitive can greatly aid the discovery of new therapeutics for RNA-mediated disease. This is particularly true for high-throughput screening of trace molecules and natural products, where the amount of model RNA and/or drug might be limited.

A canonical RNA drug target is the prokaryotic ribosomal RNA (rRNA) decoding site or A-site.[7–10] Aminoglycoside antibiotics are very effective in targeting this key functional site, disrupting protein synthesis by interfering with transfer RNA (tRNA) binding and/or reducing the codon-anticodon recognition fidelity.[11–13] The A-site is a small domain within the 16S unit of rRNA that contains two key adenine residues, A1492 and A1493 (see Figure 1). It was previously shown that a truncated RNA construct that contains the A-site region mimics the function and antibiotic recognition features of the 16S rRNA.[8,14] Fluorescence experiments using A-site constructs containing emissive and responsive nucleoside analogues such as 2-aminopurine have shown great promise,[15–18] although the fluorescence signal is antibiotic-dependent.[18–20] While alternative fluorescence assays are being developed, for example, based on Förster resonance energy transfer (FRET),[21] label-free platforms that detect an intrinsic molecular property of native RNA target/drug systems may permit greater flexibility in studying native nucleic acids and avoid probe-specific artifacts.

Nanopores are molecular Coulter counters that can analyze the properties of small molecules, polymers, and biopolymers in solution at the single-molecule level and with high-throughput (>10^4 molecules per minute).[22–25] Bayley's engineered protein channels through lipid bilayers have recently been used to discriminate among different nucleotide bases, establishing a basis for future-generation electronic DNA sequencing.[26,27] Solid-state nanopores have

* Address correspondence to wanunu@neu.edu, aksiment@illinois.edu, drndic@physics.upenn.edu.

Received for review October 21, 2010 and accepted November 8, 2011.

Published online November 08, 2011
10.1021/nn203764j

also been used for detecting complexes of DNA with small molecules[28] and biomolecules,[29−31] and other types of synthetic nanopores have been used to detect and quantify virus/antibody and protein/antibody complexation.[32−34]

We have recently demonstrated that solid-state nanopore membranes with comparable thickness to biological bilayers can distinguish between short nucleic acid polymers based on their different secondary structures.[35] Here we utilize these sensitive counters to detect and quantify the formation of a 1:1 RNA/drug complex. We demonstrate that the electronic signature of a prokaryotic 16S rRNA A-site is different when an aminoglycoside drug is bound to it, enabling electronic discrimination of the complex. Furthermore, titrating drug into the RNA molecule and counting the fraction of bound molecules as a function of drug concentration allows binding affinities to be extracted in good agreement with data generated by alternative methods. Molecular dynamics (MD) simulations that characterize the permeation of our RNA construct through nanopores with atomic resolution probe the effect of temperature, pore size, and drug binding on the ionic current signatures, which corroborates our interpretation of the measurements. These results establish that nanopores generated in thin silicon nitride membranes can be used to rapidly and accurately detect individual RNA/drug complexes.

RESULTS AND DISCUSSION

Figure 1a depicts the main features of our experimental setup. A 3 nm diameter solid-state nanopore is fabricated through an ultrathin silicon nitride membrane (8−10 nm). The nanopore acts as an electrolyte junction between the top and bottom chambers, and measuring ion current using a pair of electrodes reports the macromolecular traffic through the junction. The mean pore conductance range for pores used in this study was 4 ± 3 nS at 0 °C in 1 M KCl electrolyte, as determined from linear fits to the slopes of the $I-V$ curves in the range of ±0.5 V. Pores of this size can exhibit slight current rectification of up to 20% in the measured voltage range (*i.e.*, $0.8 < I_{+V}/I_{-V} < 1.2$), possibly due to irregular pore geometry and possible ion binding.[20]

Continuous, 2 s traces of the ion current through the pore are shown in Figure 1a, before and after the addition of A-site RNA to the negative chamber to a concentration of ∼1 μM. The steady-state open-pore current is similar after RNA addition (∼1.8 nA). A high frequency of current blockade spikes (500−2000 events/s, exact rate varies by up to 50% from pore to pore) indicates the stochastic occupancy of the pore with RNA molecules. Given the high flux, a 5−20 s trace is sufficient to collect enough information about the sample. As previously reported, the combination of a small pore diameter, an ultrathin membrane, and low bath temperature facilitates the detection of small nucleic acids.[28] Moreover, the molecular flux of short RNA fragments into the pore can be tuned by altering the voltage and the concentration of molecules in the solution. For our experiments, a voltage of 500 mV was applied in order to maximize the capture frequency and minimize the rate of unsuccessful collisions. Collisions are marked by brief and shallow current pulses, and their rate is markedly reduced when voltage is increased.[28] Occasionally, a molecule gets trapped in the pore for >100 ms, in which case voltage is reversed to eject the molecule from the pore (see Supporting Information Figures S3 and S4a).

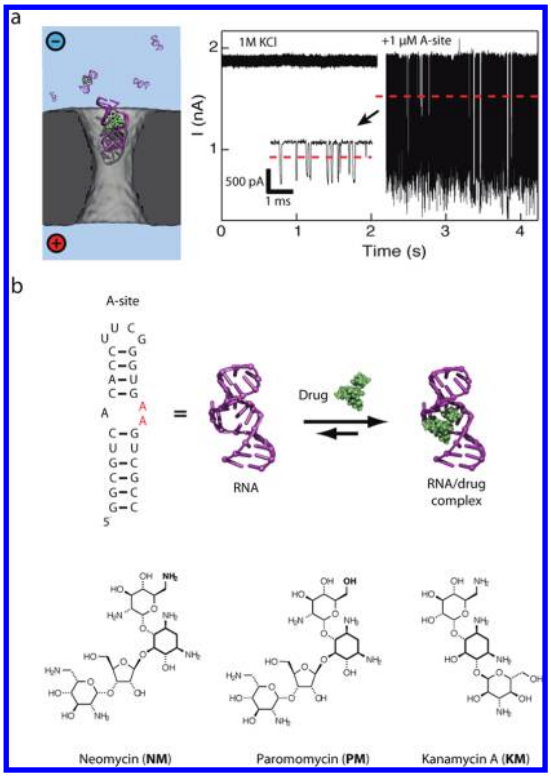

Figure 1. Counting individual RNA molecules and RNA/drug complexes using a nanopore. (a) All-atom model of a 3 nm diameter hourglass-shaped nanopore in an 8−10 nm thick silicon nitride membrane. The Si_3N_4 membrane is shown as a cut-away molecular surface, the RNA is shown in purple and aminoglycoside drug in green, and water and ions are not shown. The nanopore is the only junction between the top and bottom electrolyte chambers, each equipped with a Ag/AgCl electrode. A transmembrane voltage with a polarity indicated in the red and blue circles drives RNA molecules through the pore. Permeations of the molecules are detected as transient interruptions of the ion current. On the right, continuous ion current traces are shown before and after the addition of 1 μM A-site RNA to the negatively biased chamber. Inset shows an expanded portion of the current trace, with the appropriate scale bars. Dashed red lines indicate the threshold level used to detect the events. (b) Sequence and secondary structure of the truncated A-site model used in this study, as well as the chemical structures of the three drugs tested in this study.

Figure 1b shows the sequence and structure of the A-site construct used, where the two adjacent adenines

that constitute the active site for codon-anticodon recognition in rRNA are highlighted, and the structures of three aminoglycoside antibiotics investigated here. Although the structures of the aminoglycosides appear similar, the subtle structural differences account for vastly different affinities to the A-site RNA, as recently investigated using a novel FRET-based competition assay.[21] In going from neomycin (NM) to paromomycin (PM) to kanamycin (KM), the affinities to the A-site decrease from $IC_{50} = 7$ to 33 to 270 μM, respectively (in 500 mM NaCl, pH 8.0). Therefore, these are suitable molecules to validate our nanopore-based assay.

Figure 2 shows continuous ~200 ms ion current traces of a 3 nm diameter pore, where the negatively biased chamber contained 1 μM of A-site and PM concentrations of 0, 70, and 130 μM. The gray and pink shaded areas at the troughs of the traces are shown in order to visualize the changing characteristic current amplitude level of the events upon increasing the PM concentration. Current amplitude histograms from the experiments shown in Figure 2a are shown in Figure 2b. Each histogram is based on analysis of the mean current amplitude of thousands of events in a given experiment (the number of events *n* for each experiment is indicated in the figure; see Figure S4a in Supporting Information for complete raw data sets). Prior to the addition of PM, the distribution appears to have two predominant populations that correspond to collisions (~0.60 nA) and translocations (peak at ~0.90 nA). The green curve for the A-site fits well a double Gaussian function (see Figure S4c for exact fit parameters). As the PM concentration increases, the distribution of the current blockade amplitudes broadens, and a new population with higher ΔI emerges. This time, a triple Gaussian function was used to fit the data, and the newly emerging peak at 1.15 nA conveys the emergence of a new blockade level upon binding of PM to the A-site (see red histogram in Figure 2b, as well as scatter plots and fit parameters in Figure S4c). As more PM is added, the fraction of events with a deeper blockade is increasing, as shown by the third histogram for a PM concentration of 130 μM (purple). Exact fit parameters for all green curves are given in S4c of the Supporting Information.

Knowing the fractional occupancy of the A-site for each PM concentration, F_C, is sufficient to obtain a quantitative affinity curve, or binding isotherm. The assumption made here is that the probability of entering the pore is equal for the A-site and A-site:drug complex. We believe this to be true because the change in molecular weight upon drug binding is only <5%, and similarly, charge differences between the highly charged A-site construct and its complex are not substantial, especially at these high ionic strengths. For simple 1:1 binding, such as Drug + A → Drug:A, the dissociation constant k_d is [Drug][A]/[Drug:A], where A represents the A-site RNA. Therefore, the fraction of

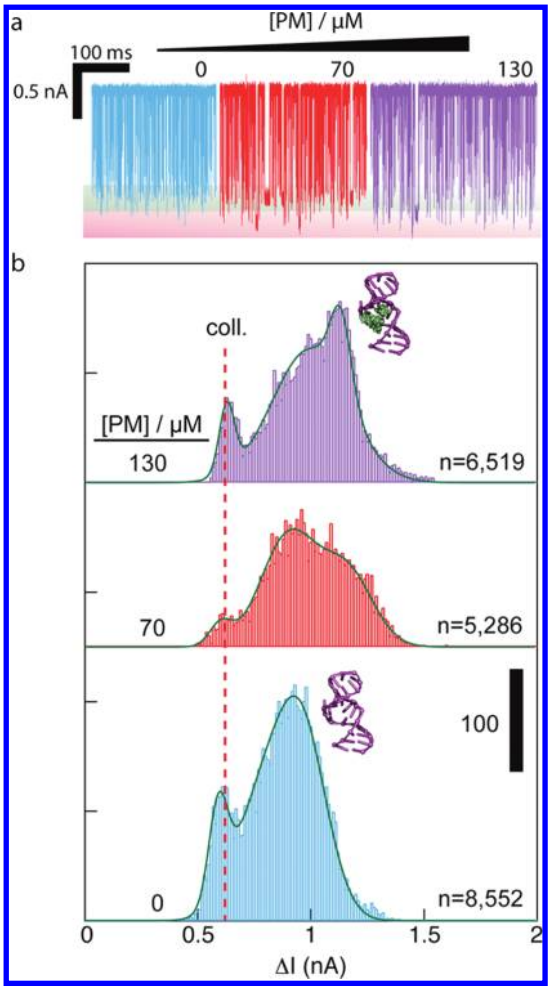

Figure 2. Ion current data report on RNA/PM complexation. (a) Three ~200 ms ion current traces recorded using a 3 nm diameter pore, 1 μM A-site and 0, 70, or 130 μM PM (shown in blue, red, and purple, respectively) added to the negatively biased chamber (see Figure S4 for >20 s traces of all data collected for each plot). The gray and pink shaded areas at the troughs of the traces are for visualization of the changing current amplitude level of the events upon increasing the PM/A-site ratio. (b) Histograms of the mean current amplitudes (ΔI). As PM concentrations increase, the fraction of PM-complexed A-site molecule increases the mean current amplitude of the events (the vertical bar represents 100 counts). The numbers of events analyzed for each histogram are indicated by the value of *n* beside it. A fraction of the events shown (up to 15%) have mean ΔI values of ~0.6 nA, which likely correspond to collisions of the RNA with the pore (see dashed red line and Figure S4 for more details). Traces were low-pass filtered to 37 kHz.

A-site molecules that form a complex with the drug $F_C \equiv$ [Drug:A]/([Drug:A] + [A]) in solution can be expressed in terms of k_d and [Drug] by

$$F_C = \frac{[\text{Drug}]}{[\text{Drug}] + k_d}$$

Ideally, free and drug-bound RNA constructs must be completely discernible in order to measure the fraction of bound molecules using the nanopore data. However, due to the overlap of current amplitudes in Figure 2, it is not straightforward to assign an exact

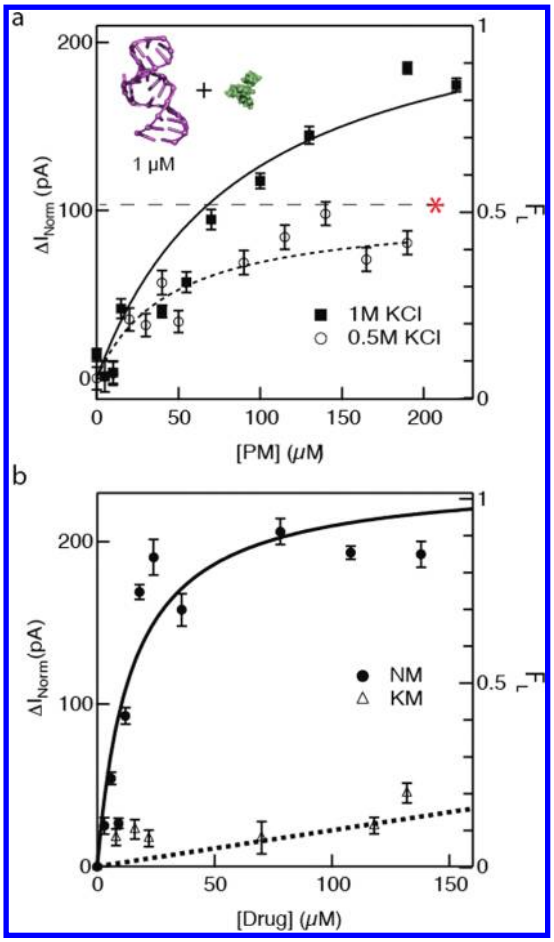

Figure 3. (a) Mean current amplitude changes (ΔI_{Norm}) for titrations of 1 μM A-site RNA with PM in 1 M KCl (solid squares) and 0.5 M KCl (open circles) at pH 7.5, 0 °C. The ΔI_{Norm} values were obtained by subtracting the ΔI value at a PM/A-site ratio of 0 (*i.e.*, A-site only). On the right axis, we plot F_L, the dimensionless loading fraction based on maximum changes to ΔI_{Norm} (see text). The dashed line and red asterisk represent F_L = 1 for the experiment with 0.5 M KCl concentration. Fitting the data points to a simple binding model yields a K_d value of 90 $\pm$ 34 μM for 1 M KCl and 44 $\pm$ 17 μM for 0.5 M KCl. (b) Mean current amplitude changes for the drugs NM and KM under identical conditions to the experiment in (a). KM does not bind to the A-site at 1 M KCl in the concentration range in which PM and NM do bind. The K_d for NM was determined to be 14.4 $\pm$ 3.3 μM.

value of F_C for each experiment (*i.e.*, for all events collected for a given sample). Even though multiple Gaussians are clearly distinguished in Figure 2b, often the populations are mixed in a way that cannot reliably yield F_C. Instead, we find that plotting the fractional change in current amplitude for all of the translocation events in each experiment can effectively quantify the fraction of bound molecules in the population. Figure 3 shows the mean current amplitude change as a function of PM concentration for two different bath salt concentrations. Each point in the graph corresponds to the mean ΔI value of $>10^3$ events at each concentration of PM, subtracted from the mean amplitude for pure A-site in the absence of PM. Dividing this ΔI_{Norm} by the value ΔI_{max} upon saturation (obtained from measurements at high drug concentrations) yields $\delta\Delta I$, a dimensionless parameter that we equate with the fraction of bound drug (*i.e.*, $\delta\Delta I \sim F_C$). For simplicity, $\delta\Delta I$ values are shown on the right axis for each trace in Figure 3. Fitting the $\delta\Delta I$ data to a simple 1:1 binding model yields a K_d value of 90 $\pm$ 34 μM at 1 M KCl and 44 $\pm$ 17 μM at 0.5 M KCl. The K_d value of 44 $\pm$ 17 μM obtained for 500 mM monovalent salt concentration compares well with an independent FRET-based assay,[21] which yielded IC_{50} of 33 $\pm$ 4 μM for PM (IC_{50} is the half maximal inhibitory concentration; see Supporting Information). The decreased affinity of A-site constructs to aminoglycosides at increased salt concentrations is clearly evident from the nanopore experiments and is attributed to electrostatic shielding effects which alter interactions of the drug with the A-site.[36] For both the 1 and 0.5 M data, the total change in the mean current amplitude at saturation corresponds to a 20−25% increase from the mean current amplitude of the free A-site, a remarkably large difference given the <5% change in molecular weight that results from complexation of A-site with an aminoglycoside.

Figure 3b shows results for NM and KM, two additional aminoglycoside antibiotics. The contrast in nanopore data between the two drugs is remarkable, although not surprising: titration of NM, which has a higher affinity to the A-site, results in an immediate increase in ΔI_{Norm} followed by saturation, while under these concentrations of the weak binder KM, there was no detectable change in ΔI_{Norm}. The binding curve for NM yielded a K_d of 14.4 $\pm$ 3.3 μM, whereas for KM, we could not extract K_d because there was no discernible binding at these concentrations. These results clearly demonstrate that nanopore current measurements are sensitive to the extent of antibiotic binding to the A-site.

Another experimental quantity collected during the nanopore measurements is the transport time of a molecule through the pore—the dwell time, measured as the duration of the ion current pulses. The dwell time depends on many factors such as the length of the nucleic acid polymer, its secondary structure, and the cross-sectional area difference between the nanopore and the nucleic acid. Therefore, quantitative measurements of the mean dwell times of the A-site upon drug binding can potentially reveal information about changes to the RNA structure induced by the drug. In Figure 4a, we present dwell-time histograms for the A-site translocation experiments under different concentrations of PM. The dwell-time distributions appear to be similar to those previously reported from the measurements of nucleic acid transport through small solid-state nanopores.[37] The most likely pulse duration is very fast (few microseconds), and the tail of the distribution can be fit to an exponential decay. Also, the mean dwell time (~40 μs) is quite similar to

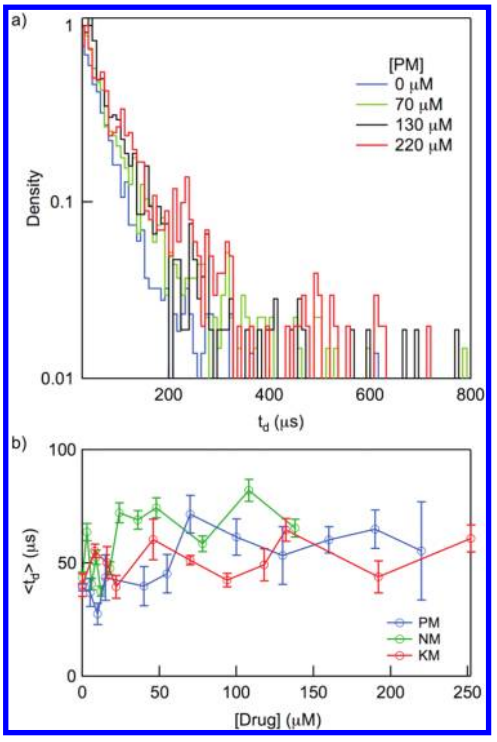

Figure 4. (a) Normalized dwell-time distributions for representative stages of the titration of A-site with PM at 1 M KCl. (b) Mean dwell times obtained from the corresponding dwell-time distributions for titrations of A-site with all three drugs (see text).

that reported in the study of probe-hybridized microRNAs, which have geometric dimensions similar to the A-site. However, there is hardly any systematic change in the mean dwell times upon binding PM, as the measured dwell-time histograms overlap. Figure 4b, which shows a plot of the mean dwell times for all of the experiments reported here, was obtained by fitting the dwell-time distributions by an exponential dependence and extracting the mean dwell times t_d. The resulting mean dwell times for all samples are in the 40−80 μs range, with no obvious systematic correlation between the mean dwell time and the fraction of drug bound. In Figure S4b, we show scatter plots of current amplitudes *versus* dwell times, which also conveys a vague correlation between F_C and dwell times.

To independently substantiate our interpretation of the ion current signals, MD simulations of electric field-driven transport of our A-site RNA construct through nanopores in Si_3N_4 membranes were performed. The sequence of snapshots in Figure 5a illustrates a simulated permeation pathway of an A-site/PM complex through a 3.2 nm diameter pore at 295 K. The blockade current and the corresponding position of the center of mass of the RNA relative to the center of the membrane are presented in Figure 5b as functions of time. The blockade current, which is defined as the ratio of the ionic current during the permeation to the open-pore current, is seen to fluctuate between 25 and 50% until the complex leaves the pore constriction and the ionic current returns to the open-pore level. In another MD trajectory featured in Figure 5b, the free RNA molecule did not permeate the nanopore within the time scale of our MD simulation, although it produced smaller current blockade amplitude than in the simulation of the A-site/PM complex.

To systematically characterize the effect of PM association with A-site RNA on the ionic current signals of the permeation events, we performed 10 independent simulations of A-site permeation through the 3.5 nm diameter pore, starting from five different initial conformations for free and PM-bound A-site. Additional eight simulations were performed to determine the effect of temperature and the pore diameter. The starting conformations of the A-site RNA constructs in the pore are described in the Supporting Information.

Figure 5c and Table 1 summarize the results of these simulations. In Figure 5c, the average blockade current is plotted *versus* the position of the A-site (open symbols) or the A-site/PM complex (filled symbols) in the nanopore for all simulations performed. The plot clearly shows that the presence of either A-site or A-site/PM complex within 3.5 nm of the membrane center substantially reduced the ionic current. The current blockade traces from individual simulations (provided in the Supporting Information) indicate significant variation of the ionic current between and within the individual runs. Furthermore, only in two 2 of 10 simulations, the A-site was observed to completely permeate the 3.5 nm diameter pore at 273 K, indicating that typical translocation times are much longer than the time scale of our MD simulations. Raising the temperature to 295 K increased the probability of observing complete permeation events; however, even at 295 K, adhesive interactions between the A-site and the pore walls arrested transport of the A-site constructs in 50% of all simulations. In two simulations of A-site/PM constructs (one each at 273 and 295 K), the complex dissociated inside the pore. Such events are likely to occur as well in experiment because of the high electrostatic force gradient in the pore constriction.[38] We observed transient enhancement of the ionic current above the open-pore level at the end of some complete permeation trajectories, associated with an increase of counterion concentration at the *trans* entrance of the pore.[39] Due to the short time scale of such events, they are unlikely to contribute to the signal measured in experiment.

To determine what effect the presence of PM has on the ionic current, we computed the average current blockade produced by the A-site or the A-site/PM complex when they resided within 3.5 nm from the center of the membrane—the ion current-modulating region of the pore (see Figure 5c). Table 1 lists the average current blockade for each simulation. Despite a considerable variation of the average blockades from

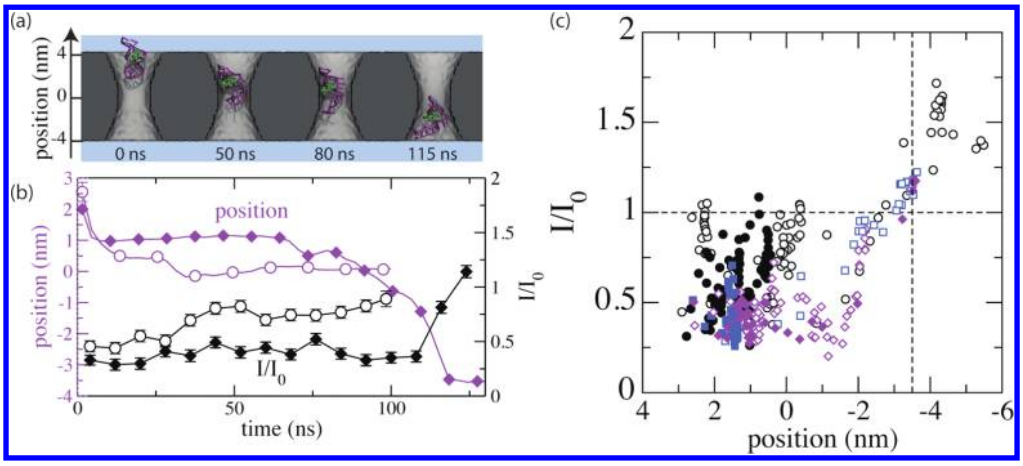

Figure 5. MD simulations of A-site construct transport through Si_3N_4 nanopores. (a) Snapshots from an MD trajectory detailing the permeation process of an A-site/PM complex. (b) Vertical position of the center of mass of the A-site construct with respect to the center of the Si_3N_4 membrane (purple, left axis) and the corresponding normalized blockade current (black, right axis). Data are shown for two MD trajectories of the A-site constructs performed with (filled symbols) and without (open symbols) PM. (c) Blockade current *vs* the vertical position of the A-site construct relative to the center of the Si_3N_4 membrane. Each data point represents the blockade current and corresponding position of the center of mass of the A-site, both averaged over a 5 ns fragment of an MD trajectory. The filled and open symbols correspond to simulations performed with and without PM. The symbols indicate different simulation conditions as follows: a 3.5 nm diameter pore at 273 K and five independent runs (circles), a 3.5 nm diameter pore at 295 K and two independent runs (squares), and a 3.2 nm diameter pore at 295 K and two independent runs (diamonds).

TABLE 1. Influence of PM Binding, Initial Conformation, Pore Diameter, and Temperature on the Simulated Ionic Current Blockades[a]

			RNA		RNA + paromomycin	
temperature (K)	pore diameter (nm)	initial conformation	current blockade (I/I_0) (%)	velocity (nm/ns)	current blockade (I/I_0) (%)	velocity (nm/ns)
273	3.5	up	68.1 ± 2	0.034	49.7 ± 1	0.017
		down	66.9 ± 2	0.149	53.5 ± 1	0.028
		horizontal	90.9 ± 2	0.0106	77.8 ± 1	0.025
		tilted up	88.7 ± 2	0.042	76.1 ± 1	0.031
		tilted down	90.9 ± 2	0.517	65.2 ± 1	0.028
295	3.5	up	92.6 ± 2	0.108	43.3 ± 1	0.014
		down	88.3 ± 2	0.142	34.8 ± 1	0.043
295	3.2	up	42.6 ± 2	0.018	43.5 ± 1	0.016
		down	51.1 ± 2	0.033	47.3 ± 1	0.049

[a] The table lists the average blockade current for each MD simulation of A-site permeation, computed over the segments of the respective MD trajectories where A-site was located within 3.5 nm from the center of the Si_3N_4 membrane. The I/I_0 values for different initial conformations of the same molecule show that different current blockade amplitudes can be obtained, predicting a broad distribution of current signals in a "real" experiment. Figures S6 and S7 in the Supporting Information detail the initial conformations of the A-site constructs, as well as the position *vs* time and blockade current *vs* time graphs for each MD run.

one simulation to the other, the average blockade currents were consistently smaller for the A-site/PM complex (*i.e.*, larger ΔI values), in agreement with our experimental blockade data. The blockade currents for A-site and A-site/PM systems averaged over the five independent simulations were 82 ± 12 and 65 ± 11%, respectively, where the standard deviation was estimated using the average values from individual runs. This large statistical uncertainty primarily originates from a large number of microscopic conformations that our A-site constructs adopted in the pore during the translocation, which we term here "conformational noise". Such conformational noise imposes a fundamental limit on the ability of a nanopore measurement to discriminate permeations of A-site from A-site/PM complex based on individual blockade events.

To elucidate the effect of PM on the ionic current blockades in the absence of the conformational noise, we carried out eight additional simulations restraining the conformations of the A-site constructs with and without PM to the NMR coordinates and placing the constructs in the pore constriction. Two possible orientations of A-site with respect to the pores were tested; the simulation systems are shown in Figure 6a,b. The table below the snapshots in Figure 6 lists the average blockade currents. For each pore and A-site conformation tested, the blockade current was significantly higher in the absence of PM. The change in the

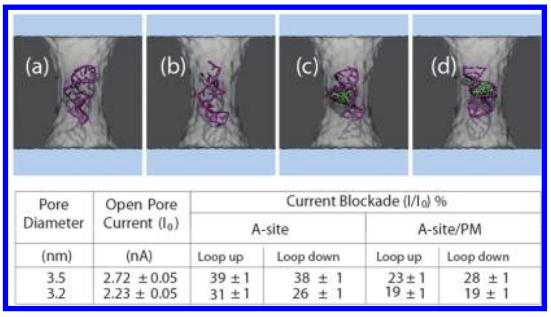

Pore Diameter	Open Pore Current (I_0)	Current Blockade (I/I_0) %			
		A-site		A-site/PM	
(nm)	(nA)	Loop up	Loop down	Loop up	Loop down
3.5	2.72 ± 0.05	39 ± 1	38 ± 1	23 ± 1	28 ± 1
3.2	2.23 ± 0.05	31 ± 1	26 ± 1	19 ± 1	19 ± 1

Figure 6. MD simulation of ionic current blockades in the absence of conformational noise. The snapshots (a–d) illustrate the conformations of the A-site (with and without PM bound) used in these simulations: "loop up" (a and c) and "loop down" (b and d). Due to harmonic restraints, the biomolecules maintained the same conformations for the entire duration of the MD run. The table lists the average open-pore and blockade currents for the two pores studied.

blockade amplitude due to PM relative to the current blockade amplitude in its absence was 18 ± 7%, where the standard deviation was computed using the current values from the four different systems.

SUMMARY AND IMPLICATIONS

The utility of ultrathin solid-state nanopores for label-free characterization of 1:1 RNA/drug complexation has been demonstrated using the prokaryotic rRNA A-site/aminoglycoside complex as a prototypical example. We first showed that upon adding a 27 nucleotide hairpin A-site model, a distinct set of current blockades corresponding to passage of the molecules through the nanopore is observed. Next, titrations of paromomycin into the A-site resulted in current blockades of larger amplitudes. By analyzing the mean current amplitudes for a population of signals at each concentration of PM, the binding equilibrium can be monitored. The binding of paromomycin to our A-site model was examined at two different salt concentrations. In line with previous reports for this particular RNA–ligand complex, and as anticipated by this largely electrostatic-driven binding phenomenon, we found that binding is weaker at higher ionic strengths. Experiments with neomycin B and kanamycin, two other A-site binding aminoglycoside antibiotics, that stronger and weaker affinities can be resolved using our system, further supporting the correlation between the blockade current amplitude and drug binding. Our MD simulations independently support that the average signal amplitude is a function of aminoglycoside binding to the A-site. Quantitatively, the experimentally measured differences in blockade current amplitudes upon binding of PM (20–25%) are quite similar to the results of the simulations that yielded the difference of 18 ± 7%. The results presented here demonstrate that affinities at the single-complex level can be measured, also conveying the broad range of utility and applicability of sub-10 nm thick nanopores for studying various nucleic acid/drug systems.

METHODS

Experiments. Nanopores with diameters of 3 ± 0.3 nm were fabricated as previously described[28] in 8–10 nm thick low-stress silicon nitride membranes supported by a 5 × 5 mm^2 Si chip. The chips were cleaned using piranha and then assembled in a custom fluoropolymer cell that utilizes a silicone elastomer seal between the chip and the cell, such that the nanopore is the only interface between two electrolyte solutions. The cell was mounted on a thermistor-equipped copper block for feedback temperature control, allowing the temperature to be regulated to within 0.1 °C. The details of our experimental setup and ultrathin nanopore device fabrication are described elsewhere.[28]

The truncated A-site RNA construct used in this study was a 27 nucleotide hairpin-forming sequence 5′-GGCGUCACAC-CUUCGGGUGAAGUCGCC, purchased from Integrated DNA Technologies. The RNA was purified by gel electrophoresis and then desalted on a Sep-Pak (Waters Corporation). Paromomycin sulfate (PM), kanamycin sulfate (KM), and neomycin sulfate (NM), were purchased from Sigma-Aldrich and converted into the corresponding neutral form by passing through DOWEX MONOSPHERE 550 Å (OH) anion exchange resin. Prior to titrations, RNA solutions prepared using RNase-free water were heated to 75 °C for 5 min, cooled to room temperature over 2 h, and placed on ice for 30 min.

All nanopore experiments were carried out at 0 °C in order to facilitate nanopore detection of the RNA complex, provide a pseudosterile environment that minimizes RNA degradation, and minimize solvent evaporation. A total of 10 pores were used for experiments presented here, and for these pores, the current signal amplitudes and dwell-time durations were reproduced to within 30%. For every experiment, a free A-site RNA was used initially to confirm pore functionality.

In a typical titration, 100 μL of electrolyte buffered to pH 7.5 was placed in the analyte chamber along with ~100 pmol of the A-site construct. After mixing the solution and allowing 2 min for equilibration, voltage was applied across the nanopore using the Axopatch amplifier and ~20 s long continuous current data were recorded to allow 10^3–10^4 events to be collected. All experiments were performed using an applied voltage of 500 mV to improve the capture efficiency of the molecules into the pore.[28] Drug solution was then titrated into the analyte chamber followed by ~2 min equilibration and data recording. This process was repeated until the anticipated titration end point. The current signal was low-pass filtered using the 100 kHz Bessel filter of the Axopatch and sampled at 250 kS/s using a digital acquisition board (National Instruments). Data analysis was performed using custom LabVIEW software that detects data points below a threshold of 0.8*$\langle I_{open} \rangle$ and assigns for each event a mean current amplitude ($\Delta I = \langle I_{open} \rangle - \langle I_{event} \rangle$) and duration ($t_d$). Collisions were excluded from analysis of average ΔI by only including events with ΔI > 0.7 nA. Fractions of bound drug were calculated as described in the Results and Discussion section.

Simulations. All MD simulations were carried out using NAMD,[40] periodic boundary conditions, the particle mesh Ewald electrostatics,[41] and multiple time-stepping[42] wherein local interactions were calculated every time step and full electrostatic evaluations performed every three time steps. A 2 fs integration time step was used with RATTLE[43] and SETTLE[44] algorithms applied to covalent bonds involving hydrogens in water and RNA/PM, respectively. The van der Waals forces were evaluated using a cutoff of 8 Å and a switching distance of 7 Å. The CHARMM27[45] force field was used for nucleic acids, water, and ions along with the custom force field for the Si_3N_4

membrane[46] and the CHARMM-compatible parameters for PM.[47] The NpT simulations were carried out using the Nosé-Hoover Langevin piston pressure control,[48] and the temperature in the NVT simulations was maintained using a Langevin thermostat with the damping constant of 1.0 ps^{-1} applied to all atoms of the Si_3N_4 membrane. In all simulations, the bulk and surface atoms of the Si_3N_4 membrane were harmonically restrained with the spring constants of 695 and 6950 pN/nm, respectively.

All-atom models of our experimental system were created by removing atoms from an 8 nm thick Si_3N_4 membrane, as previously described.[49] Two hourglass pores with minimum diameter of 3.5 and 3.2 nm, respectively, were constructed to have their narrowest parts located at the center of the membrane. The microscopic models of the A-site constructs with and without bound PM were based on the NMR structure[50] (protein data bank entry code 1PBR). The RNA or RNA/PM complex was then placed near the entrance of the nanopore (see Figure 1a), and the resulting system was submerged in a volume of pre-equilibrated TIP3P water.[51] K^+ and Cl^- ions were added at random positions to a concentration of 1 M; additional K^+ ions were then added to bring the net charge of the system to zero. The final systems had the shape of a hexagonal prism with a side length of 9.2 nm and a thickness of 22 nm and contained approximately 158 000 atoms. For the simulations of the open-pore current, two additional systems were built containing no RNA or RNA/PM constructs.

After initial energy minimization, the systems were equilibrated for 300 ps having all C atoms of the A-site construct harmonically restrained, followed by a 1 ns equilibration in the absence of any restraints. All subsequent simulations were performed at constant volume. A constant external electric field was applied that corresponds to a transmembrane bias of 300 mV. The stability of our models of the RNA and RNA/drug constructs in the absence of the nanopore membrane and applied electric field was tested in separate simulations that are detailed in the Supporting Information. The ionic currents were computed as previously described.[52] A detailed description of our simulation protocols was recently reported.[53]

Acknowledgment. This work was supported by grants from the National Institutes of Health (HG 004767 to M.D.; HG 005115 and P41-RR005969 to A.A.; GM 069773 to Y.T.), and National Science Foundation (DMR-095595 and PHY-0822613). The authors acknowledge supercomputer time provided by the National Institute for Computational Sciences *via* Teragrid Resources Allocation Grant No. MCA05S028.

Supporting Information Available: Fluorescence titration curves of a A-site analogue with paromomycin at 500 mM KCl; a 20 s nanopore current *vs* time trace; raw data and scatter plots for A-site titration with PM; details about the MD simulations. This material is available free of charge *via* the Internet at http://pubs.acs.org.

REFERENCES AND NOTES

1. Osborne, R. J.; Thornton, C. A. RNA-Dominant Diseases. *Hum. Mol. Genet.* **2006**, *15*, R162–R169.
2. Cooper, T. A.; Wan, L. L.; Dreyfuss, G. RNA and Disease. *Cell* **2009**, *136*, 777–793.
3. O'Rourke, J. R.; Swanson, M. S. Mechanisms of RNA-Mediated Disease. *J. Biol. Chem.* **2009**, *284*, 7419–7423.
4. Vicens, Q. RNA's Coming of Age as a Drug Target. *J. Incl. Phenom. Macrocycl. Chem.* **2009**, *65*, 171–188.
5. Borman, S. Targeting RNA. *Chem. Eng. News* **2009**, *87*, 63–66.
6. Higgins, C. F. Multiple Molecular Mechanisms for Multidrug Resistance Transporters. *Nature* **2007**, *446*, 749–757.
7. Vicens, Q.; Westhof, E. Crystal Structure of Paromomycin Docked into the Eubacterial Ribosomal Decoding A-Site. *Structure* **2001**, *9*, 647–658.
8. Hermann, T. A-Site Model RNAs. *Biochimie* **2006**, *88*, 1021–1026.
9. Tor, Y. The Ribosomal A-Site as an Inspiration for the Design of RNA Binders. *Biochimie* **2006**, *88*, 1045–1051.
10. Tor, Y. Exploring RNA−Ligand Interactions. *Pure & Appl. Chem.* **2009**, *81*, 263−272.
11. Moazed, D.; Noller, H. F. Interaction of Antibiotics with Functional Sites in 16S Ribosomal-RNA. *Nature* **1987**, *327*, 389–394.
12. Lynch, S. R.; Gonzalez, R. L.; Puglisi, J. D. Comparison of X-Ray Crystal Structure of the 30S Subunit-Antibiotic Complex with NMR Structure of Decoding Site Oligonucleotide-Paromomycin Complex. *Structure* **2003**, *11*, 43–53.
13. Llano-Sotelo, B.; Klepacki, D.; Mankin, A. S. Selection of Small Peptides, Inhibitors of Translation. *J. Mol. Biol.* **2009**, *391*, 813–819.
14. Purohit, P.; Stern, S. Interactions of a Small RNA with Antibiotic and RNA Ligands of the 30S Subunit. *Nature* **1994**, *370*, 659–662.
15. Parsons, J.; Hermann, T. Conformational Flexibility of Ribosomal Decoding-Site RNA Monitored by Fluorescent Pteridine Base Analogues. *Tetrahedron* **2007**, *63*, 3548–3552.
16. Barbieri, C. M.; Kaul, M.; Pilch, D. S. Use of 2-Aminopurine as a Fluorescent Tool for Characterizing Antibiotic Recognition of the Bacterial rRNA A-Site. *Tetrahedron* **2007**, *63*, 3567–3574.
17. Shandrick, S.; Zhao, Q.; Han, Q.; Ayida, B. K.; Takahashi, M.; Winters, G. C.; Simonsen, K. B.; Vourloumis, D.; Hermann, T. Monitoring Molecular Recognition of the Ribosomal Decoding Site. *Angew. Chem., Int. Ed.* **2004**, *43*, 3177–3182.
18. Kaul, M.; Barbieri, C. M.; Pilch, D. S. Fluorescence-Based Approach for Detecting and Characterizing Antibiotic-Induced Conformational Changes in Ribosomal RNA: Comparing Aminoglycoside Binding to Prokaryotic and Eukaryotic Ribosomal RNA Sequences. *J. Am. Chem. Soc.* **2004**, *126*, 3447–3453.
19. Chao, P. W.; Chow, C. S. Monitoring Aminoglycoside-Induced Conformational Changes in 16S rRNA through Acrylamide Quenching. *Bioorg. Med. Chem.* **2007**, *15*, 3825–3831.
20. Srivatsan, S. G.; Tor, Y. Fluorescent Pyrimidine Ribonucleotide: Synthesis, Enzymatic Incorporation, and Utilization. *J. Am. Chem. Soc.* **2007**, *129*, 2044–2053.
21. Xie, Y.; Dix, A. V.; Tor, Y. FRET Enabled Real Time Detection of RNA-Small Molecule Binding. *J. Am. Chem. Soc.* **2009**, *131*, 17605–17614.
22. Bezrukov, S. M.; Vodyanoy, I.; Parsegian, V. A. Counting Polymers Moving through a Single-Ion Channel. *Nature* **1994**, *370*, 279–281.
23. Kasianowicz, J. J.; Brandin, E.; Branton, D.; Deamer, D. W. Characterization of Individual Polynucleotide Molecules Using a Membrane Channel. *Proc. Natl. Acad. Sci. U.S.A.* **1996**, *93*, 13770–13773.
24. Gu, L. Q.; Braha, O.; Conlan, S.; Cheley, S.; Bayley, H. Stochastic Sensing of Organic Analytes by a Pore-Forming Protein Containing a Molecular Adapter. *Nature* **1999**, *398*, 686–690.
25. Akeson, M.; Branton, D.; Kasianowicz, J. J.; Brandin, E.; Deamer, D. W. Microsecond Time-Scale Discrimination among Polycytidylic Acid, Polyadenylic Acid, and Polyuridylic Acid as Homopolymers or as Segments within Single RNA Molecules. *Biophys. J.* **1999**, *77*, 3227–3233.
26. Astier, Y.; Braha, O.; Bayley, H. Toward Single Molecule DNA Sequencing: Direct Identification of Ribonucleoside and Deoxyribonucleoside 5′-Monophosphates by Using an Engineered Protein Nanopore Equipped with a Molecular Adapter. *J. Am. Chem. Soc.* **2006**, *128*, 1705–1710.
27. Clarke, J.; Wu, H. C.; Jayasinghe, L.; Patel, A.; Reid, S.; Bayley, H. Continuous Base Identification for Single-Molecule Nanopore DNA Sequencing. *Nat. Nanotechnol.* **2009**, *4*, 265–270.
28. Wanunu, M.; Dadosh, T.; Ray, V.; Jin, J.; McReynolds, L.; Drndic, M. Rapid Electronic Detection of Probe-Specific MicroRNAs Using Thin Nanopore Sensors. *Nat. Nanotechnol.* **2010**, *5*, 807–814.
29. Tabard-Cossa, V.; Wiggin, M.; Trivedi, D.; Jetha, N. N.; Dwyer, J. R.; Marziali, A. Single-Molecule Bonds Characterized by

Solid-State Nanopore Force Spectroscopy. *ACS Nano* **2009**, *3*, 3009–3014.
30. Kowalczyk, S. W.; Hall, A. R.; Dekker, C. Detection of Local Protein Structures along DNA Using Solid-State Nanopores. *Nano Lett.* **2010**, *10*, 324–328.
31. Singer, A.; Wanunu, M.; Morrison, W.; Kuhn, H.; Frank-Kamenetskii, M.; Meller, A. Nanopore Based Sequence Specific Detection of Duplex DNA for Genomic Profiling. *Nano Lett.* **2010**, *10*, 738–742.
32. Uram, J. D.; Ke, K.; Hunt, A. J.; Mayer, M. Label-Free Affinity Assays by Rapid Detection of Immune Complexes in Submicrometer Pores. *Angew. Chem., Int. Ed.* **2006**, *45*, 2281–2285.
33. Uram, J. D.; Ke, K.; Hunt, A. J.; Mayer, M. Submicrometer Pore-Based Characterization and Quantification of Antibody−Virus Interactions. *Small* **2006**, *2*, 967–972.
34. Sexton, L. T.; Horne, L. P.; Sherrill, S. A.; Bishop, G. W.; Baker, L. A.; Martin, C. R. Resistive-Pulse Studies of Proteins and Protein/Antibody Complexes Using a Conical Nanotube Sensor. *J. Am. Chem. Soc.* **2007**, *129*, 13144–13152.
35. Wanunu, M.; Sutin, J.; Meller, A. DNA Profiling Using Solid-State Nanopores: Detection of DNA-Binding Molecules. *Nano Lett.* **2009**, *9*, 3498–3502.
36. Pilch, D. S.; Kaul, M.; Barbieri, C. M. Ribosomal RNA Recognition by Aminoglycoside Antibiotics. In *DNA Binders and Related Subjects*; Springer-Verlag: Berlin, 2005; Vol. 253, pp 179−204.
37. Wanunu, M.; Sutin, J.; McNally, B.; Chow, A.; Meller, A. DNA Translocation Governed by Interactions with Solid-State Nanopores. *Biophys. J.* **2008**, *95*, 4716–4725.
38. Heng, J. B.; Aksimentiev, A.; Ho, C.; Marks, P.; Grinkova, Y. V.; Sligar, S.; Schulten, K.; Timp, G. Stretching DNA Using the Electric Field in a Synthetic Nanopore. *Nano Lett.* **2005**, *5*, 1883–1888.
39. Comer, J.; Dimitrov, V.; Zhao, Q.; Timp, G.; Aksimentiev, A. Microscopic Mechanics of Hairpin DNA Translocation through Synthetic Nanopores. *Biophys. J.* **2009**, *96*, 593–608.
40. Phillips, J. C.; *et al.* Scalable Molecular Dynamics with NAMD. *J. Comput. Chem.* **2005**, *26*, 1781–1802.
41. Darden, T.; York, D.; Pedersen, L. Particle Mesh Ewald - An N.LOG(N) Method for Ewald Sums in Large Systems. *J. Chem. Phys.* **1993**, *98*, 10089–10092.
42. Batcho, P. F.; Case, D. A.; Schlick, T. Optimized Particle-Mesh Ewald/Multiple-Time Step Integration for Molecular Dynamics Simulations. *J. Chem. Phys.* **2001**, *115*, 4003–4018.
43. Andersen, H. C. RATTLE - A Velocity Version of the SHAKE Algorithm for Molecular-Dynamics Calculations. *J. Comput. Phys.* **1983**, *52*, 24–34.
44. Miyamoto, S.; Kollman, P. A. SETTLE - An Analytical Version of the SHAKE and RATTLE Algorithm for Rigid Water Models. *J. Comput. Chem.* **1992**, *13*, 952–962.
45. MacKerell, A. D.; *et al.* All-Atom Empirical Potential for Molecular Modeling and Dynamics Studies of Proteins. *J. Phys. Chem. B* **1998**, *102*, 3586–3616.
46. Heng, J. B.; Aksimentiev, A.; Ho, C.; Marks, P.; Grinkova, Y. V.; Sligar, S.; Schulten, K.; Timp, G. The Electromechanics of DNA in a Synthetic Nanopore. *Biophys. J.* **2006**, *90*, 1098–1106.
47. Romanowska, J.; Setny, P.; Trylska, J. Molecular Dynamics Study of the Ribosomal A-Site. *J. Phys. Chem. B* **2008**, *112*, 15227–15243.
48. Martyna, G. J.; Tobias, D. J.; Klein, M. L. Constant-Pressure Molecular-Dynamics Algorithms. *J. Chem. Phys.* **1994**, *101*, 4177–4189.
49. Aksimentiev, A.; Heng, J. B.; Timp, G.; Schulten, K. Microscopic Kinetics of DNA Translocation through Synthetic Nanopores. *Biophys. J.* **2004**, *87*, 2086–2097.
50. Fourmy, D.; Recht, M. I.; Blanchard, S. C.; Puglisi, J. D. Structure of the A-Site of *Escherichia coli* 16S Ribosomal RNA Complexed with an Aminoglycoside Antibiotic. *Science* **1996**, *274*, 1367–1371.
51. Jorgensen, W. L.; Chandrasekhar, J.; Madura, J. D.; Impey, R. W.; Klein, M. L. Comparison of Simple Potential Functions for Simulating Liquid Water. *J. Chem. Phys.* **1983**, *79*, 926–935.
52. Aksimentiev, A.; Schulten, K. Imaging α-Hemolysin with Molecular Dynamics: Ionic Conductance, Osmotic Permeability, and the Electrostatic Potential Map. *Biophys. J.* **2005**, *88*, 3745–3761.
53. Aksimentiev, A. Deciphering Ionic Current Signatures of DNA Transport through a Nanopore. *Nanoscale* **2010**, *2*, 468–483.